Sheath fold development in monoclinic shear zones

Marta Adamuszek[1], Marcin Dabrowski[1,2]

[1] Computational Geology Laboratory, Polish Geological Institute – National Research Institute, Wrocław, Poland

[2] Physics of Geological Processes, University of Oslo, Norway

Abstract

We use numerical simulations to investigate the evolution of sheath folds around slip surfaces in simple shear dominated monoclinic shear zones. A variety of sheath fold shapes develops under general shear, including tubular folds with low aspect ratio eye patterns and tongue-like structures showing bivergent flanking structures in sections normal to the sheath elongation, which may potentially lead to confusing shear sense interpretations. Not all investigated monoclinic flow end-members lead to the development of sheath folds *sensu stricto* (folds with apical angle <90°). The aspect ratio of the eye patterns, R_{yz}, correlates with the ratio between the principal strain in the Y-direction and the smaller of the principal strains in the X-Z plane and thus it could be used in strain analysis.

1. Introduction

Sheath folds are a special kind of non-cylindrical folds, which are characterized by a sharp bend of the hinge line (e.g., Carreras, et al., 1977, Quinquis, et al., 1978). Ramsay and Huber (1987) defined sheath folds as folds with a minimum hinge angle (the apical angle) not exceeding 90° (Fig. 1 D). Sheath folds occur across a wide range of scales in various rock types such as metamorphic rocks, soft sediments, glaciotectonic sediments, evaporites, or ignimbrites (Alsop, et al., 2007 and references therein). In the field, they are typically recognized based on distinctive elliptical eye patterns in cross-sections perpendicular to the sheath elongation. Sheath folds can develop in pure shear flow (e.g., Ghosh and Sengupta, 1984), however, due to their common occurrence in high strain shear zones, their formation is often associated with simple shear dominated flow regimes (Cobbold and Quinquis, 1980). Passive amplification of the original layer perturbations (Cobbold and Quinquis, 1980, Holdsworth, 1990), and flow perturbation due to the presence of rigid inclusions (Marques and Cobbold, 1995), basement corrugations (Cobbold and Quinquis, 1980), or slip surfaces (Reber, et al., 2012) have been suggested among various mechanisms of sheath fold formation in simple shear.

Several authors have indicated that simple shear alone cannot explain the great variety of sheath fold morphologies observed in nature (e.g., Alsop and Holdsworth, 2006, Jiang and Williams, 1999). Alsop and Holdsworth (2006) presented a detailed geometric analysis of sheath folds occurring in general shear zones. They analysed sheath folds developing in three shear regimes categorized based on the Flinn's k-value of the strain ellipsoid, namely: 1) plane strain (k=1), 2) flattening strain (k<1), and 3) constrictional strain (k>1). The authors demonstrated that the ratio of the longest to shortest axis of the outermost elliptical contour (R_{yz}) (Fig. 1E) shows a decreasing trend with increasing k-value.

The analysis of shear zones reveals that ideal simple shear conditions are rare and, general shear prevails instead (Simpson and Depaor, 1993). Two- and three-dimensional theoretical flow models have been developed to study structure development under general shear conditions (e.g., Passchier, 1998, Tikoff and Fossen, 1999). While most studies focus on monoclinic deformation, some authors suggest that triclinic shear may be more widespread than previously considered (Jiang and Williams, 1998). The development of sheath folds due to amplifying layer perturbations in triclinic flows was examined theoretically by Jiang and Williams (1999), who showed that the fold evolution strongly depends on the flow type and the initial shape of the perturbation.

We present a numerical study of sheath fold development in a layered, albeit homogeneous matrix around a slip surface subject to a monoclinic shear in the far field. We examine the evolution of sheath fold shapes for a range of coaxial to non-coaxial deformation rates and compare our results with the natural data presented by Alsop and Holdsworth (2006). The purpose of this study is to gain insight into sheath fold development in general shear and validate their potential use as the strain magnitude and regime indicator.

2. Mechanical Model

We study a three-dimensional mechanical model of sheath fold formation around a pre-existing, initially circular slip surface embedded in a homogeneous, isotropic, linear viscous matrix (Exner and Dabrowski, 2010, Reber, Dabrowski and Schmid, 2012). We obtain the velocity field using the external Eshelby solution (Eshelby, 1959), which is modified to the case of an incompressible viscous matrix and an elliptical and inviscid inclusion. The model is subject to an incompressible, monoclinic, non-spinning flow in the far field. We use a Cartesian reference frame XYZ (Fig. 1), which coincides with the principal directions of a superimposed coaxial flow component. The X-direction is the shear direction of the background simple shear and the vorticity vector is parallel to the Y-axis (Fig. 1A). For each model, we calculate the three orthogonal eigenvectors of the rate of deformation tensor, which are referred to as the instantaneous stretching axes (ISA_1, ISA_2, and ISA_3). Due to a monoclinic character of the flow, ISA_3 coincides with the Y-direction and the two others lay in the X-Z plane. We also find the three flow asymptotes (or fabric attractors) (AP), which are the eigenvectors of the velocity gradient tensor. The flow asymptotes AP give the directions of material lines irrotational with respect to ISA and also uniquely describe the flow pattern in the model (Passchier, 1997). For the studied flows, there are two asymptotes coinciding with the X- and Y-directions and a third asymptote is lying in the X-Z plane at an angle θ to the X-direction. The asymptote inclination is a function of the kinematic vorticity number (W_k) (Bobyarchick, 1986), which is a measure of the relative contribution of the coaxial and non-coaxial flow components (Ghosh, 1987, Passchier, 1986).

A circular slip surface with radius r_0 is prescribed in the model centre perpendicular to ISA_2, which corresponds to a mode I fracture. The slip surface behaves as a passive element, and, with strain, it synthetically rotates and stretches into an ellipse (Means, 1989).

Following the approach of Tikoff and Fossen (1999), we distinguish 12 end-member models based on characteristics of the superposed coaxial component. In our naming convention, the shortening direction of the coaxial component is indicated after letter S and the extension direction after T, e.g., SX-TY. We recognize the same configuration between the crack and the flow asymptotes in the following model pairs 1) SX-TZ and SZ-TX, 2) SXY-TZ and SYZ-TX, 3) SY-TZ and SY-TX, 4) SZ-TXY and SX-TYZ, 5) SZ-TY and SX-TY (Fig. 1C). Thus, there are only 7 unique end-member setups and we choose the ones, in which AP_2 coincides with X-direction. In addition, we use the simple shear flow S0-R0 as a reference model (Fig. 1C).

In our numerical simulations, a simple shear rate of $\dot{\gamma} = 1$ is used and the coaxial flow rate is set to $\dot{\varepsilon} = 0.05,\ 0.075,\ \text{and}\ 0.1$. The maximum stretch obtained after $\gamma=30$ due to coaxial deformation is ca. 4.5, 9.5, and 20.1, respectively. In the case of models with shortening or extension taking place simultaneously in two directions (e.g. SXY-TZ, SX-TYZ), the rate is halved in these directions. The kinematic vorticity number is equal to 1 for S0-T0 and it is not less than 0.98 in the other models. Structure evolution is tracked using regularly spaced passive marker planes, which are initially parallel to the X-Y foliation plane. The deformation leads to the development of sheath folds, whose geometry is analysed for shear strain $\gamma = 5,\ 10,\ 15,\ 25,\ \text{and}\ 30$. The analysis of the aspect ratio (R_{yz}) is carried out in the sections normal to the X-direction at the locations, where the investigated interfaces form the outermost closed contour of the eye-structure.

3. Results

3.1. A detailed analysis of SY-TX, S0-T0, and SZ-TY models

For detailed analysis, we select the SY-TX, S0-T0, and SZ-TY models that correspond to the constrictional, plane strain, and flattening strain regimes discussed by Alsop and Holdsworth (2006). Fig. 2A shows the fold shapes at γ=15, using $\dot{\varepsilon}/\dot{\gamma} = 0.05$ for SY-TX and SZ-TY. The central X-Z section showing flanking structures and Y-Z sections with eye patterns are presented in Fig. 2B and C, respectively. In the SY-TX model, a narrow tubular-shaped sheath fold develops, forming almost circular closed contours in the Y-Z sections. In the S0-T0 model, the sheath fold exhibits a tongue-like shape, with noticeably non-concentric, asymmetric ellipses developing in the Y-Z cross-section past the crack tip. The shape asymmetry is greater in the sections closer to the crack tip. In the SZ-TY model, the hinge line is gently curved, the fold is strongly flattened, and the eye-patterns are characterized by large aspect ratios. The interfaces around the eye structure form a double vergent structure (Alsop and Holdsworth, 2004), which is also referred to as an anvil shape (Mies, 1993) or an omega shape pattern (Reber, Dabrowski and Schmid, 2012). In the Y-Z sections intercepting the crack, the structure resembles bivergent flanking structures, which is also manifested in the contour depression developed above the crack.

We analyse the impact of $\dot{\varepsilon}/\dot{\gamma}$ on the sheath structure developing in a selected interface (z_0/r_0=0.82) for the SY-TX and SZ-TY models. In Fig. 3, we plot R_{yz} as a function of $\dot{\varepsilon}/\dot{\gamma}$ for different γ. We use thick dashed lines to indicate the fold structure, in which the apical angle is smaller than 90°. Increasing $\dot{\varepsilon}/\dot{\gamma}$ causes R_{yz} to decrease in SY-TX and to increase in SZ-TY models. In both models, the slope is steeper for larger γ. In SY-TX, large $\dot{\varepsilon}/\dot{\gamma}$ prevents sheath fold to develop, whereas, in SZ-TY, it significantly widens the apical angle and, thus, inhibits the development of sheath folds *sensu stricto* for most of the $\dot{\varepsilon}/\dot{\gamma}$ and γ value sets.

3.2. R_{yz} scaling with strain

In our results generated using three $\dot{\varepsilon}/\dot{\gamma}$ for six γ in all the models, we observe R_{yz} values between $3 \cdot 10^{-1}$ and $6 \cdot 10^{2}$. For the plane strain models (k=1), R_{yz} is not below 4, it is not larger than 6 in the constrictional models (k>1), whereas, for flattening models (k<1), it is always above 3. In Fig. 4A, we use a log-log scale plot to show R_{yz} as a function of the Flinn's k-value for different δ and γ. We consider data from all the sections with closed contours, irrespective of whether intercepted interfaces form sheath fold *sensu stricto* or not. We also plot the field data of Alsop and Holdsworth (2006) (their Fig. 8g). Both field and numerical data show a generally decreasing trend of R_{yz} with increasing k. For large k values, the trend is perturbed due to a switch of the direction between the intermediate and minor principal axis of the strain ellipsoid (Fossen and Tikoff, 1993). The diagram, which we selected to present the data, lumps various plane strain models (k=1), which show a scatter of R_{yz}. Field and numerical data show a satisfactory overlap, although, no natural data are available for very small and large k-values.

A significantly better numerical data collapse is observed in Fig. 4B, which shows R_{yz} as a function of the ratio between the principal strain in the Y-direction and the smaller of the principal strains measured in the X-Z plane ($\tilde{\lambda}_2/\tilde{\lambda}_3$). A good correlation between R_{yz} and $\tilde{\lambda}_2/\tilde{\lambda}_3$ occurs for $\tilde{\lambda}_2/\tilde{\lambda}_3 < 3$, with a slope equal to 1 in the log-log plot. For $\tilde{\lambda}_2/\tilde{\lambda}_3 > 3$, the slope varies between 1/2 and 1 depending on the model and the data collapse is slightly less prominent. In both figures, we mark in grey a field of high (>30) and low (<1/30) values of R_{yz}, k, and $\tilde{\lambda}_2/\tilde{\lambda}_3$, for which obtaining natural data can be challenging.

4. Discussion

Our numerical simulations of sheath fold development around slip surfaces show that they can develop for a wide spectrum of monoclinic flows. The coaxial flow component significantly influences the fold shape, leading to the development of structures exhibiting shapes between narrow finger-like and wide tongue-like (Fig. 2). The unusual eye patterns observed for SZ-TY model, which appeared as bivergent flanking structures, may lead to incorrect shear sense determination, if only a part of the structure is visible. We note that the coaxial component of a large magnitude can suppress sheath fold development (Fig. 3).

The complex geometry of the developing sheath folds hampers the direct adaptation of the approach presented by Adamuszek and Dabrowski (in press), in which the early fold shape is fitted with a horizontally oriented cone, and the R_{yz} evolution with strain can be approximated using an analytical expression. The observed correlation between R_{yz} and $\tilde{\lambda}_2/\tilde{\lambda}_3$ is not unexpected, however, an explanation to why the slope varies between 1/2 and 1 should be offered. In our view, it may result from a different dependence on the simple and pure shear deformation components. For simple shear, Adamuszek and Dabrowski (in press) showed that R_{yz} scales as $\sqrt{\gamma}$ for large strain, which approximately gives a slope of 1/2 if R_{yz} is plot as a function of $\tilde{\lambda}_2/\tilde{\lambda}_3$, whereas for pure shear, the correlation between R_{yz} and $\tilde{\lambda}_2/\tilde{\lambda}_3$ is expected to be linear.

We have compared the field data presented by Alsop and Holdsworth (2006) to our numerical results (Fig. 4A). The results generally support the findings of Alsop and Holdsworth (2006) on the correlation between R_{yz} and strain. However, R_{yz} values obtained in the numerical simulations cover a wider range than the available measurements of natural sheath fold. High R_{yz} values can be difficult to measure in nature (Skjernaa, 1989) and, for the same reason, very small or large k-values might be systematically over- or underestimated. The observed deviations between the field and numerical data can also be related to simplified geometry and rheological behaviour used in our model, whereas rocks in shear zones are often heterogeneous, anisotropic, and nonlinear (Cook, et al., 2014, Dabrowski and Schmid, 2011, Schmalholz and Schmid, 2012). In our analysis, we have focused on sheath folds developing around slip surface, but we acknowledge that various other mechanisms may lead to the sheath fold formation. The good fit between the model results and field observations (Fig. 4A and B) supports the current model, but it also suggests that similar correlations may apply to sheath folds in general, irrespectively of their formation mechanism.

Reber et al. (2013) showed that closed contours with $R_{yz}<3$ are difficult to generate in simple shear deformation, even if the initial orientation and aspect ratio of the slip surface is varied. Alsop and Holdsworth (2006) suggested that $R_{yz}<3$ is generally obtained in the constrictional deformation. The shortening component acting in the Y-direction clearly promotes small R_{yz} values (Fig. 4). However, $R_{yz}<3$ is achieved only in SY-TX and SY-TXZ, whereas in SYZ-TX it is above 3. Moreover, the overlap of the data from all the deformation groups for $R_{yz}>3$ indicates that R_{yz} cannot be used as a reliable discriminator of the bulk strain type in this range. On the other hand, a reasonable correlation of the R_{yz} data with $\tilde{\lambda}_2/\tilde{\lambda}_3$ shows that the aspect ratios of the closed contours in sheath folds could be used in the strain analysis of shear zones to estimate the relative deformation in the out-of-plane Y-direction.

5. Conclusions

A variety of sheath fold shapes can be generated due to deformation around slip surfaces under general shear. The contribution of the coaxial component may lead to eye patterns with low aspect ratio. Complex structures resembling bivergent flanking structures may develop in Y-Z sections, potentially resulting in confusing shear sense determination. Not all flow conditions lead to the development of sheath folds *sensu stricto*. The aspect ratio (R_{yz}) of the closed contours observed in the sections normal to the shearing direction correlates with the ratio between the principal strain in the Y-direction (out-of-simple shear plane) and the smaller of the principal strains measured in the X-Z plane. The documented correlation between the two parameters over a few orders of magnitude, allows for strain estimation based on R_{yz}.

6. Acknowledgements

The project has been funded by the National Science Centre, based on the decision number DEC-2013/11/D/ST10/03458. MD acknowledges the Polish Geological Institute research project no. 61.9015.1601.00.0. We thank Barbara Senderak for drafting the figures and helpful discussions.

7. References

Adamuszek, M. and Dabrowski, M., 2017. Sheath folds as a strain gauge in simple shear *Journal of Structural Geology*, **102**, 21-36.

Alsop, G.I. and Holdsworth, R.E., 2004. The geometry and topology of natural sheath folds: a new tool for structural analysis *Journal of Structural Geology*, **26**, 1561-1589.

Alsop, G.I. and Holdsworth, R.E., 2006. Sheath folds as discriminators of bulk strain type *Journal of Structural Geology*, **28**, 1588-1606.

Alsop, G.I., Holdsworth, R.E. and McCaffrey, K.J.W., 2007. Scale invariant sheath folds in salt, sediments and shear zones *Journal of Structural Geology*, **29**, 1585-1604.

Bobyarchick, A.R., 1986. The Eigenvalues of Steady Flow in Mohr Space *Tectonophysics*, **122**, 35-51.

Carreras, J., Estrada, A. and White, S., 1977. Effects of Folding on C-Axis Fabrics of a Quartz Mylonite *Tectonophysics*, **39**, 3-24.

Cobbold, P.R. and Quinquis, H., 1980. Development of Sheath Folds in Shear Regimes *Journal of Structural Geology*, **2**, 119-126.

Cook, A.C., Vel, S.S., Gerbi, C. and Johnson, S.E., 2014. Computational analysis of nonlinear creep of polyphase aggregates: Influence of phase morphology *Journal of Geophysical Research: Solid Earth*, **119**, 6877-6906.

Dabrowski, M. and Schmid, D.W., 2011. A rigid circular inclusion in an anisotropic host subject to simple shear *Journal of Structural Geology,* **33**, 1169-1177.

Eshelby, J.D., 1959. The elastic field outside an ellipsoidal inclusion *Proceeding of the Royal Society of London Series a-Mathematical and Physical Sciences*, **252**, 561-569.

Exner, U. and Dabrowski, M., 2010. Monoclinic and triclinic 3D flanking structures around elliptical cracks *Journal of Structural Geology*, **32**, 2009-2021.

Fossen, H. and Tikoff, B., 1993. The Deformation Matrix for Simultaneous Simple Shearing, Pure Shearing and Volume Change, and Its Application to Transpression Transtension Tectonics *Journal of Structural Geology*, **15**, 413-422.

Ghosh, S.K., 1987. Measure of Non-Coaxiality *Journal of Structural Geology*, **9**, 111-113.

Ghosh, S.K. and Sengupta, S., 1984. Successive Development of Plane Noncylindrical Folds in Progressive Deformation *Journal of Structural Geology*, **6**, 703-709.

Holdsworth, R.E., 1990. Progressive Deformation Structures Associated with Ductile Thrusts in the Moine Nappe, Sutherland, N Scotland *Journal of Structural Geology*, **12**, 443-452.

Jiang, D.Z. and Williams, P.F., 1998. High-strain zones: a unified model *Journal of Structural Geology*, **20**, 1105-1120.

Jiang, D.Z. and Williams, P.F., 1999. When do dragfolds not develop into sheath folds in shear zones? *Journal of Structural Geology*, **21**, 577-583.

Marques, F.G. and Cobbold, P.R., 1995. Development of Highly Noncylindrical Folds around Rigid Ellipsoidal Inclusions in Bulk Simple Shear Regimes - Natural Examples and Experimental Modeling *Journal of Structural Geology*, **17**, 589-&.

Means, W.D., 1989. Stretching Faults *Geology*, **17**, 893-896.

Mies, J.W., 1993. Structural-Analysis of Sheath Folds in the Sylacauga-Marble-Group, Talladega Slate Belt, Southern Appalachians *Journal of Structural Geology*, **15**, 983-993.

Passchier, C.W., 1986. Flow in Natural Shear Zones - the Consequences of Spinning Flow Regimes *Earth and Planetary Science Letters*, **77**, 70-80.

Passchier, C.W., 1997. The fabric attractor *Journal of Structural Geology*, **19**, 113-127.

Passchier, C.W., 1998. Monoclinic model shear zones *Journal of Structural Geology*, **20**, 1121-1137.

Quinquis, H., Audren, C., Brun, J.P. and Cobbold, P.R., 1978. Intense Progressive Shear in Ile De Groix Blueschists and Compatibility with Subduction or Obduction *Nature*, **273**, 43-45.

Ramsay, J.G. and Huber, M.I., 1987. *The techniques of modern structural geology. Volume 2: Folds and fractures*. Academic Press, London; New York.

Reber, J.E., Dabrowski, M. and Schmid, D.W., 2012. Sheath fold formation around slip surfaces *Terra Nova*, **24**, 417-421.

Schmalholz, S.M. and Schmid, D.W., 2012. Folding in power-law viscous multi-layers *Philosophical Transactions of the Royal Society a-Mathematical Physical and Engineering Sciences*, **370**, 1798-1826.

Simpson, C. and Depaor, D.G., 1993. Strain and Kinematic Analysis in General Shear Zones *Journal of Structural Geology*, **15**, 1-20.

Skjernaa, L., 1989. Tubular Folds and Sheath Folds - Definitions and Conceptual Models for Their Development, with Examples from the Grapesvare Area, Northern Sweden *Journal of Structural Geology*, **11**, 689-703.
Tikoff, B. and Fossen, H., 1999. Three-dimensional reference deformations and strain facies *Journal of Structural Geology*, **21**, 1497-1512.

Figure captions

Fig. 1. A) Schematic illustration of SZ-TX model showing the far-field flow conditions. ISA_1 and ISA_2, are the two instantaneous shortening axes and the two material line attractors are denoted AP_1 and AP_2. The ISA_3 and AP_3 axes and the vorticity vector are orthogonal to the X-Z plane (monoclinic flow). B) Numerical setup: a circular slip surface located in the model centre at an angle θ to the steady-state AP_2-AP_3 foliation plane. The crack is initially perpendicular to ISA_2. C) Schematic illustration of simple shear (reference model S0-T0) and 7 end-member monoclinic flows used in the study (see text for details). D) Three-dimensional sketch illustrating the apical angle of a sheath. E) Diagram showing the aspect ratio of the outermost closed contour of the eye pattern.

Fig. 2. A) 3D visualization of the sheath folds for SY-TX, S0-T0, and SZ-TY models after shear strain γ=15. We use $\dot{\varepsilon}/\dot{\gamma} = 0.05$ in SY-TX and SZ-RY. The same uppermost marker plane is used in all the models. a-a', b-b', and c-c' show the locations of the Y-Z sections used in C. B) X-Z cross-sections showing flanking structures. C) Y-Z cross-sections showing eye patterns. Red lines show the intercepting slip surface.

Fig. 3. Aspect ratio of the outermost closed contour (R_{yz}) as a function of the ratio between the rate of coaxial deformation to the shearing rate ($\dot{\varepsilon}/\dot{\gamma}$) for A) SY-TX and B) SZ-TY models. The markers at the end of the line indicate the largest $\dot{\varepsilon}/\dot{\gamma}$ for a given γ, for which the closed contours are observed. Dashed lines are used for sheath structures, in which the apical angle is smaller than 90°.

Fig. 4. A) Simulation results and field measurements (after Alsop and Holdsworth, 2006) showing relation between the aspect ratio of the outermost closed contour (R_{yz}) and the

k-value. B) Numerical data showing R_{yz} as a function of the ratio between the principal strain along the Y-direction and the smaller of the principal strains measured in the X-Z plane (see text for details).

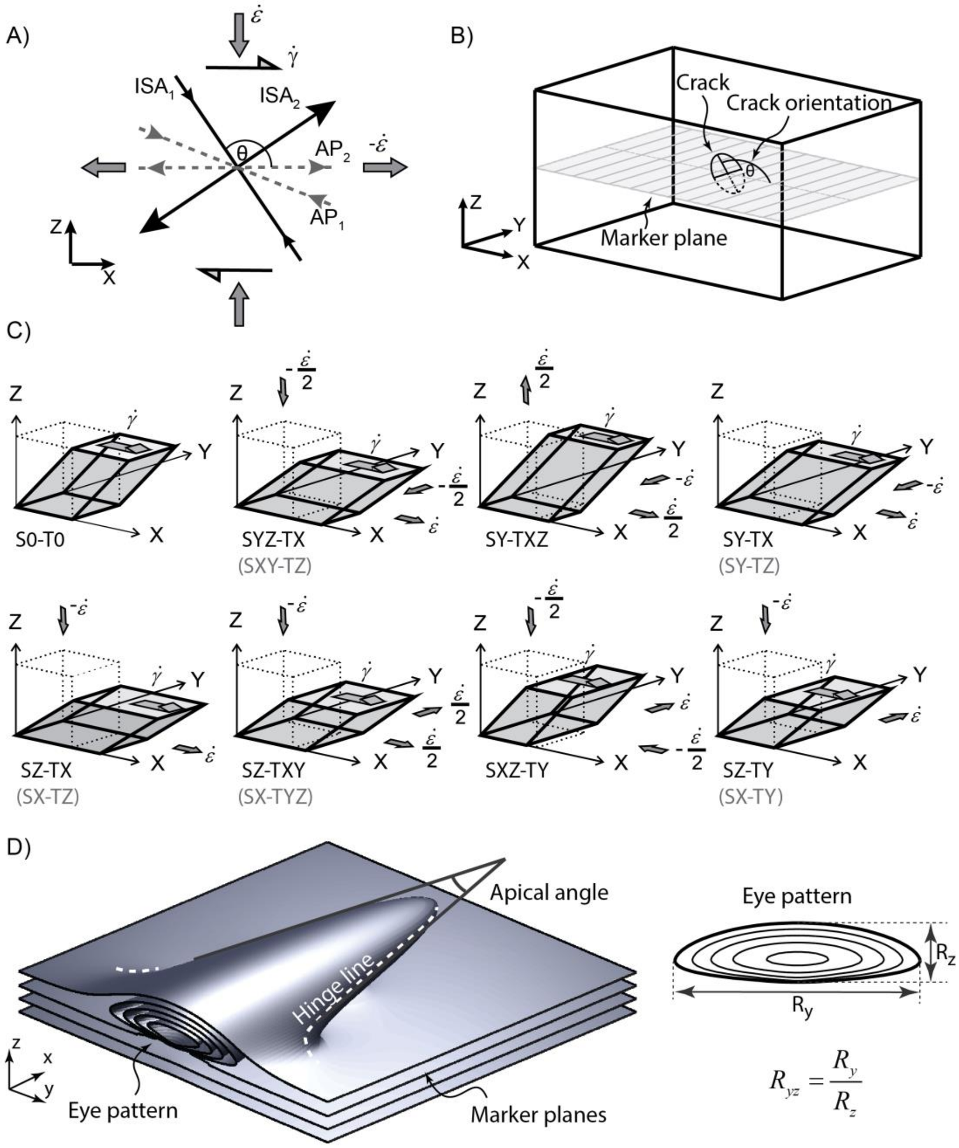
A)
ISA1
ISA2
AP2
AP1
θ
B)
Crack
Crack orientation
θ
Marker plane
C)
S0-T0
SYZ-TX
(SXY-TZ)
SY-TXZ
SY-TX
(SY-TZ)
SZ-TX
(SX-TZ)
SZ-TXY
(SX-TYZ)
SXZ-TY
SZ-TY
(SX-TY)
D)
Apical angle
Hinge line
Eye pattern
Marker planes
Eye pattern
Rz
Ry
$R_{yz} = \frac{R_y}{R_z}$

305

306 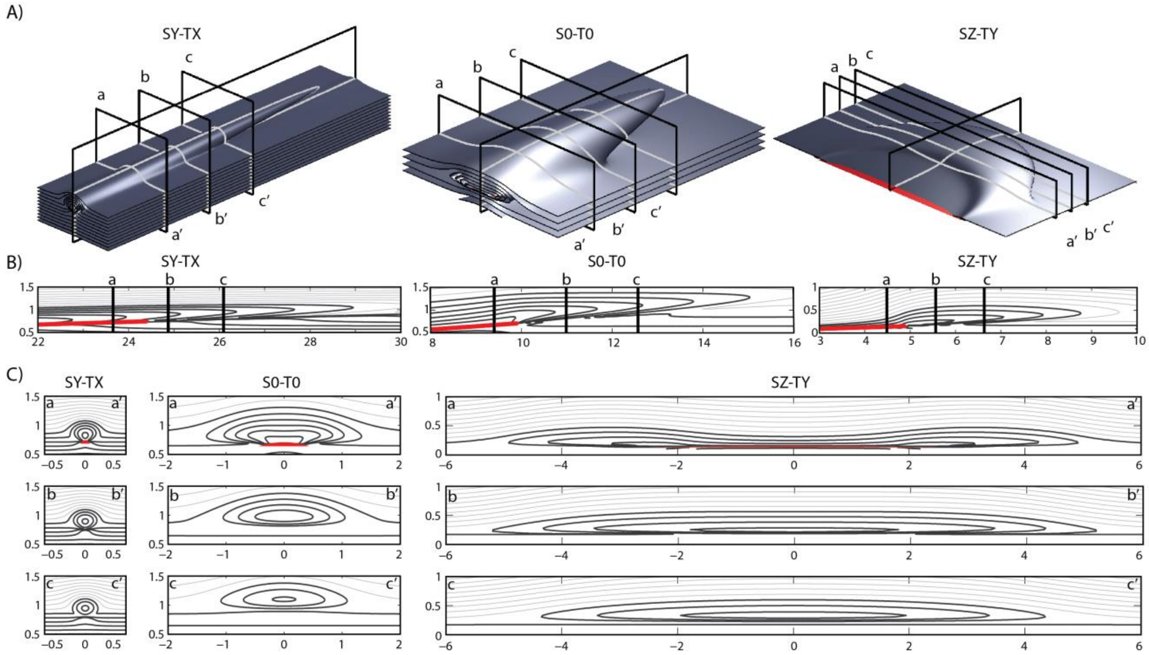

A)
SY-TX
S0-T0
SZ-TY
a
b
c
a′
b′
c′
B)
C)

307 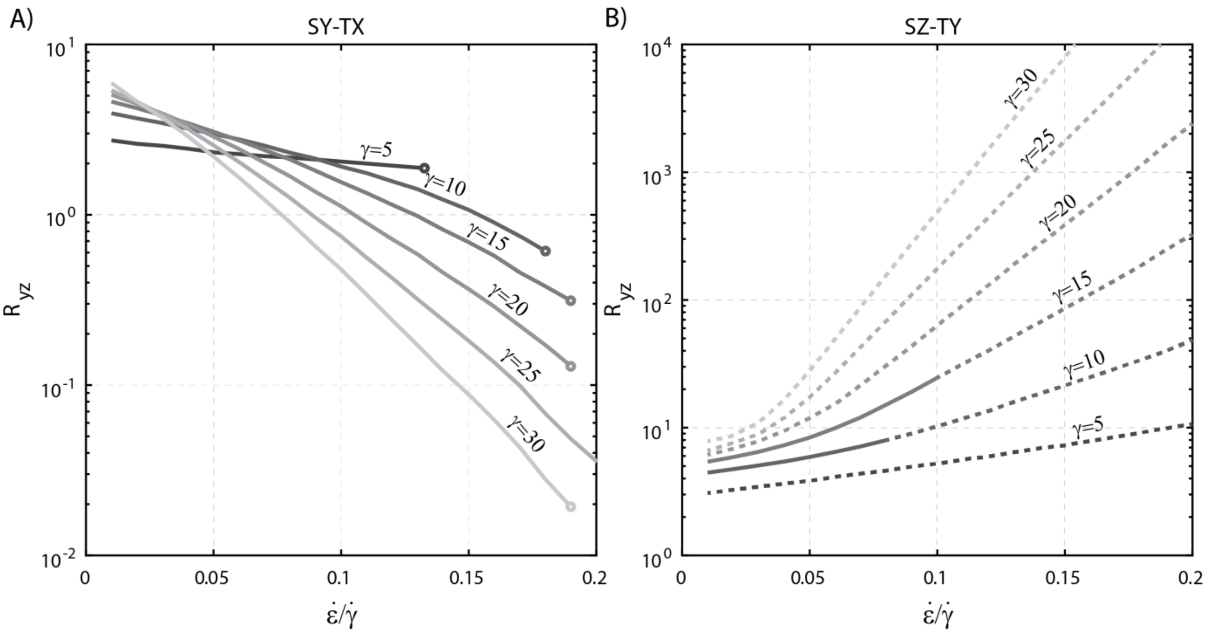

A)
SY-TX
B)
SZ-TY
R_{yz}
$\dot{\varepsilon}/\dot{\gamma}$
γ=5
γ=10
γ=15
γ=20
γ=25
γ=30

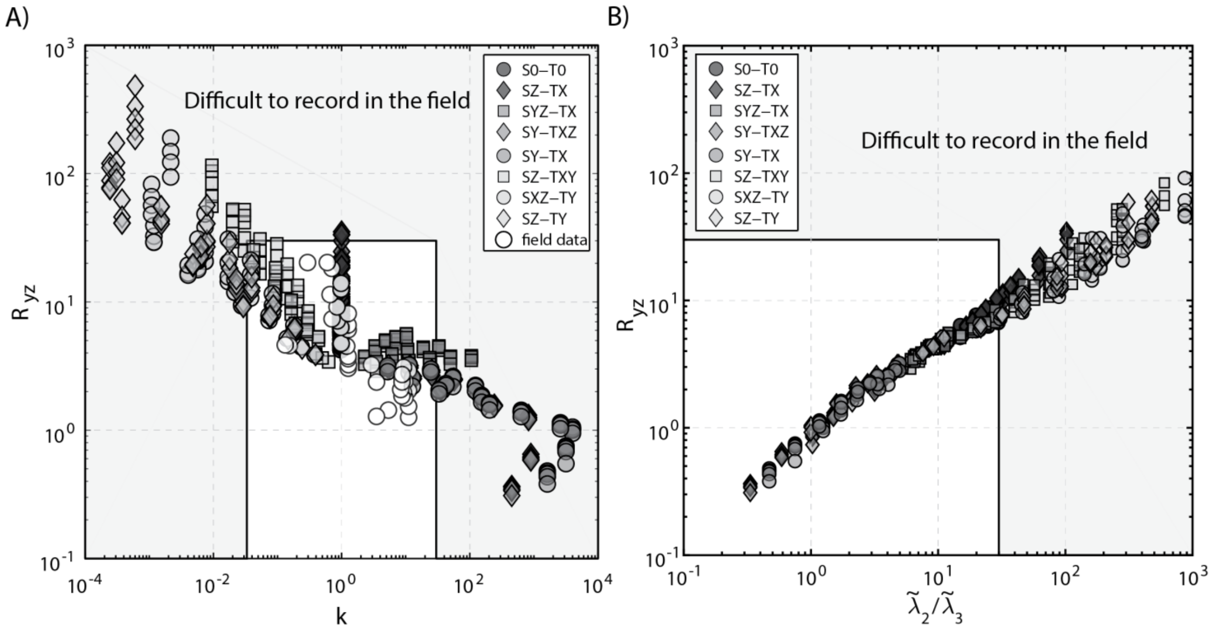
A)
Difficult to record in the field
S0–T0
SZ–TX
SYZ–TX
SY–TXZ
SY–TX
SZ–TXY
SXZ–TY
SZ–TY
field data
R_{yz}
k
B)
Difficult to record in the field
S0–T0
SZ–TX
SYZ–TX
SY–TXZ
SY–TX
SZ–TXY
SXZ–TY
SZ–TY
R_{yz}
$\tilde{\lambda}_2/\tilde{\lambda}_3$